

From Symmetry to Stability: Structural and Electronic Transformation in Cs_2KInI_6

Mohammad Bakhsh,^{1,*} Victor Trinquet,¹ Rogério Almeida Gouvêa,¹ Gian-Marco Rignanese,^{1,2} and Samuel Poncé^{1,2,†}

¹ *UCLouvain, Institute of Condensed Matter and Nanosciences (IMCN),*

Chemin des Étoiles 8, B-1348 Louvain-la-Neuve, Belgium

² *WEL Research Institute, avenue Pasteur 6, 1300 Wavre, Belgium.*

(Dated: February 9, 2026)

Cs_2KInI_6 is a promising lead-free halide double perovskite with a calculated direct band gap of 1.24 eV, ideal for solar cell applications. Our first-principles calculations reveal that its cubic phase ($\text{Fm}\bar{3}\text{m}$) is dynamically unstable. Using an accelerated machine learning approach, we identify 42 dynamically stable structures and further validate these findings using first-principles calculations on 11 of these. The most stable phase has Cmc_2_1 symmetry with 20 atoms/unit cell. It lies 41.9 meV/atom below the cubic reference but lacks octahedral cation coordination. The most stable perovskite-like structure has $\text{P}\bar{3}$ symmetry with 10 atoms/unit cell and low octahedral connectivity. Structure-property trade-offs are highlighted, with calculated distortions generally widening the band gap, shifting it from direct to indirect, and flattening the band edges. This work showcases the synergy of genetic algorithms, machine-learned potentials, and first-principles validation for discovering stable, complex materials.

Halide perovskites have attracted significant attention for solar cell applications due to their tunable band gap [1], high absorption coefficient [2] and low-cost solution-based processability [3]. As a result, the power conversion efficiency of single-junction halide perovskite solar cells has increased rapidly, reaching 27% in a short period [4]. However, most high-performance halide perovskites, such as the organic-inorganic hybrid methylammonium (MA) lead halides [5–7] and inorganic cesium lead halides [8], contain toxic lead, which poses serious environmental and health concerns that hinder large-scale commercialization [9]. In addition, these materials often suffer from limited environmental stability [10, 11]. These challenges have prompted researchers to explore the broader chemical space in search of lead-free and more stable halide perovskite alternatives. In particular, lead-free halide double perovskites with the general formula $\text{A}_2\text{MM}'\text{X}_6$ have emerged as promising candidates for photovoltaic applications [12–14]. These structures are derived by doubling the formula unit of the conventional single perovskite APbX_3 (X being an halogen) and replacing the two lead cations with two different metal cations, M and M'. These substituting cations may both adopt a +2 oxidation state, or one may be +1 and the other +3, so that their combined charge is equivalent to that of two Pb^{2+} ions. Ideally with a ns^2 -type cation, which typically shows enhanced optical absorption, well-balanced carrier transport, good defect tolerance, and long carrier diffusion lengths [15]. This substitution scheme significantly expands the accessible chemical space compared to APbX_3 perovskites. Such perovskites have been reported to exhibit improved thermal and moisture stability compared to hybrid perovskites

such as $(\text{MA})\text{PbI}_3$. In particular, $\text{Cs}_2\text{AgBiBr}_6$ demonstrates improved durability and defect tolerance [12].

However, it has an indirect band gap [16], which limits its effectiveness in photovoltaic applications [14]. To find better candidates, Cai *et al.* [17] performed a high-throughput study and reported the Cs_2KInI_6 perovskite but filtered it out due to its high energy above the convex hull (56 meV/atom) [18]. In a more recent work, its cubic phase was identified as a promising candidate for photovoltaic applications among 1026 compounds [19] due to its direct band gap that matches optimal sunlight absorption. Nevertheless, its vibrational dynamical stability was not investigated. In this work, we study the dynamical stability of Cs_2KInI_6 in the cubic phase with space group $\text{Fm}\bar{3}\text{m}$ (225). Our phonon analysis reveals that this high-symmetry phase is dynamically unstable, leading to 42 more stable phases with lower symmetry. In the cubic phase, both K and In cations occupy octahedral coordination environments. These octahedra are corner-sharing, forming a three-dimensional alternating network. The dynamically stable phases are analyzed on the basis of the possible modification of the local environments of the K and In cations and the polyhedra connectivity, which has a significant impact on transport properties [20]. Furthermore, the impact of these structural transformations on electronic properties is evaluated to estimate the suitability of this material for photovoltaic applications.

The initial crystal structure of cubic Cs_2KInI_6 was obtained from the Materials Project database [18]. Electronic structure calculations were performed using density functional theory (DFT) [21, 22] as implemented in the QUANTUM ESPRESSO (QE) package [23]. The Perdew–Burke–Ernzerhof (PBE) [24] exchange-correlation functional was used with norm-conserving pseudopotentials from the PSEUDO DOJO library [25]. After performing convergence tests on total energy per atom, lattice constants, and atomic po-

* mohammad.bakhsh@uclouvain.be

† samuel.ponce@uclouvain.be

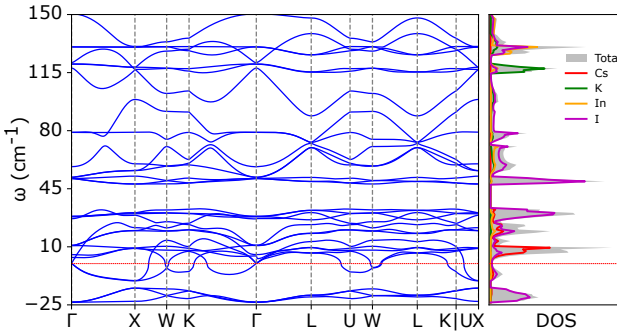


FIG. 1. Phonon dispersion and phonon density of states (DOS) for cubic Cs_2KInI_6 (space group $\text{Fm}\bar{3}\text{m}$, 225), computed using density functional perturbation theory with a $3 \times 3 \times 3$ \mathbf{k} -point grid and $2 \times 2 \times 2$ \mathbf{q} -point grid.

sitions, the plane-wave kinetic energy cutoff was set to 80 Ry. The convergence thresholds were chosen to be 0.1 mHa/atom for total energy and 0.1% of the converged value for lattice constants and atomic positions. The Brillouin zone was sampled using a $3 \times 3 \times 3$ Γ -centered Monkhorst-Pack [26] \mathbf{k} -point mesh. Structural optimization was performed with a force convergence threshold of 10^{-5} Ry/bohr. Phonon calculations were performed using density functional perturbation theory (DFPT) [27, 28] for high-accuracy validation, using \mathbf{q} -point grids with a density below $(0.5/\text{\AA})^3$ [29] and a \mathbf{k} -point mesh denser or equal to the corresponding \mathbf{q} -point grid. For high-throughput analysis, phonons were computed using the finite-displacement method with a machine-learned interatomic potential (MLIP) based on the message-passing atomic cluster expansion (MACE), specifically the MACE-OMAT-0 model [30, 31], with phonon frequencies converged to within 2 cm^{-1} . Structural analysis was performed using CHEMENV [32] to determine the coordination environments of K and In cations.

Figure 1 shows the phonon dispersion and phonon density of states (DOS) of cubic Cs_2KInI_6 using DFPT. The presence of unstable modes indicates that this high-symmetry phase lies at a saddle point on the potential energy surface [33], reflecting its dynamical instability. Although such an instability can sometimes be stabilized by including anharmonic effects at finite temperature [34], it is useful to identify the ground-state structure from DFT to describe perovskites at cryogenic temperatures or in situations where the high-symmetry phase cannot be stabilized.

To achieve this, a MACE potential was used with our in-house code called VIBROML [35] to explore the complex potential energy surface of the Cs_2KInI_6 structure. To resolve its dynamical instabilities, we use a genetic algorithm for a global search aimed at identifying dynamically stable low-energy polymorphs in the energy landscape of the material. The procedure begins by identifying the soft phonon modes of the unstable cubic phase. An initial population of distorted candidate structures

is then generated by displacing atoms along the eigenvectors of these unstable modes. This initial generation explores various displacement amplitudes and coupling with other soft modes to ensure a diverse search space. The algorithm then proceeds through an iterative evolutionary cycle. At each generation, the fitness of every candidate structure is evaluated on the basis of its total energy per atom after a structural relaxation using the MACE potential. The candidates with the lowest energies are preferentially selected as parents for the next generation. New offspring structures are created using genetic operators such as crossover, which combines features from parent structures, and mutation, which applies small, random perturbations. This process, inspired by natural selection, effectively navigates the energy landscape toward more stable configurations.

Crucially, the workflow incorporates a feedback loop: a phonon calculation is performed on the most promising low-energy candidates of each generation. If any instabilities persist, the corresponding soft modes are used to guide the creation of new distorted structures in subsequent iterations. This evolutionary approach allows for a broad and efficient search that systematically uncovers lower-energy, dynamically stable polymorphs originating from the unstable parent structure. This process yielded 42 new polymorphs of Cs_2KInI_6 , which were found to be dynamically stable based on frozen-phonon calculations using MACE (see Table S1 of the Supplemental Information, SI). They can be classified according to the number of atoms in their primitive unit cell (10, 20, 40, and 80 atoms). From this set, we selected all polymorphs with 10 atoms, two with 20 atoms (one perovskite structure and the most stable non-perovskite structure), one with 40 atoms, and the one for the 80 atoms count. This resulted in a total of 11 structures for which DFPT phonon calculations were performed. We found that in 9 cases the DFPT calculations confirmed the dynamic stability predicted by MACE, whereas in two cases MACE predicted stability but DFPT revealed dynamical instabilities. In addition, some polymorphs of Cs_2KInI_6 were predicted to be dynamically unstable by both MACE and DFPT; these structures are listed in Table S2. Overall, the DFPT phonon dispersions and phonon densities of states show very good agreement with the corresponding MACE results (see Figs. S1–S3 and S5–S6 for phonon dispersions, and Figs. S4 and S7 for phonon densities of states in the SI).

For the rest of this work, we chose to analyze four structures with $\text{id}=05, 07, 37$ and 42 in more detail. The $\text{P}\bar{3}$ (147) structure ($\text{id}=05$) with 10 atoms per unit cell and a double perovskites structure; the $\text{I}\bar{4}2\text{m}$ (121) structure ($\text{id}=07$) which is the most stable structure with 10 atoms and high symmetry; the $\text{Cmc}2_1$ (36) structure ($\text{id}=37$) as the most stable; and the $\text{P}\bar{1}$ (2) structure ($\text{id}=42$) which is the largest structure with 80 atoms per unit cell. We report their lattice parameters, number of atoms in the primitive unit cell, and relative total energies per atom (with respect to the cubic phase) in Table I.

TABLE I. Lattice parameters (constants a , b , and c in Å; angles α , β , and γ in $^\circ$) of the conventional unit cell, number of atoms in the primitive unit cell (N_{at}), and relative total energy (ΔE) for the dynamically stable DFPT polymorphs of Cs_2KInI_6 . ΔE is given with respect to the cubic $\text{Fm}\bar{3}\text{m}$ (225) phase and expressed in meV/atom.

Space group	id	a	b	c	α	β	γ	N_{at}	ΔE	
$\text{Fm}\bar{3}\text{m}$	225	00	12.669	12.669	12.669	90.0	90.0	90.0	10	0.0
$\text{P}3$	147	05	8.649	8.649	8.595	90.0	90.0	120.0	10	-30.8
$\text{I}\bar{4}2\text{m}$	121	07	7.756	7.756	19.018	90.0	90.0	90.0	10	-34.2
$\text{Cmc}2_1$	36	37	10.644	19.482	10.299	90.0	90.0	90.0	20	-41.9
$\text{P}\bar{1}$	2	42	17.427	17.502	17.662	91.7	119.0	119.1	80	-30.4

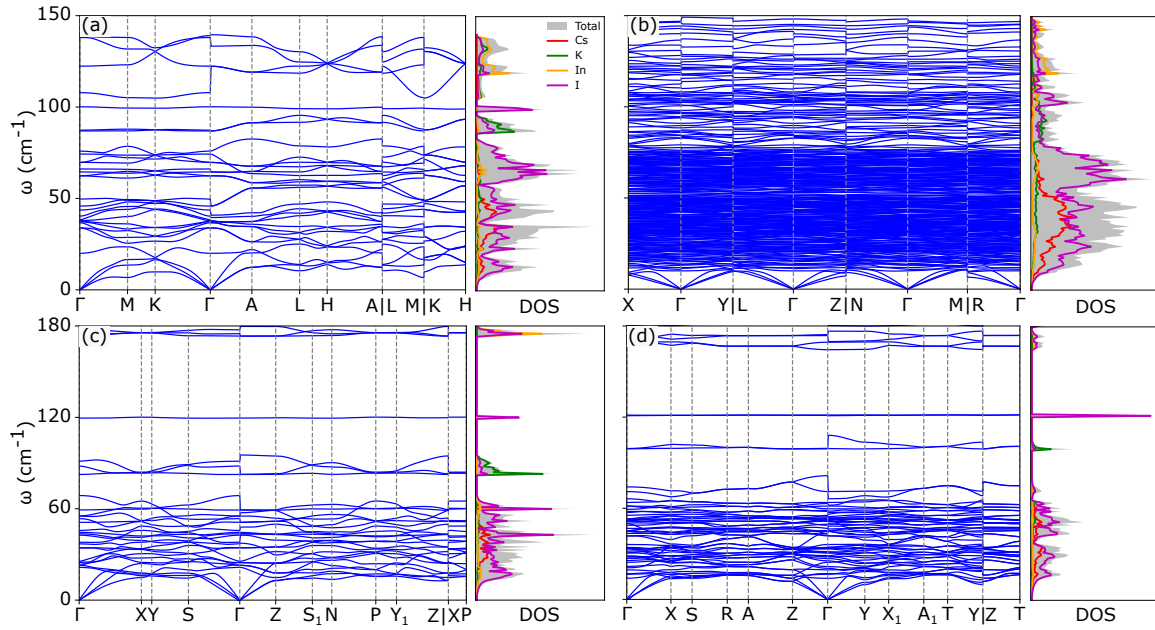


FIG. 2. DFPT phonon calculations with density of states (DOS) of four Cs_2KInI_6 phases. (a) $\text{P}3̄$ with $4 \times 4 \times 4$ \mathbf{k} -grid and $2 \times 2 \times 2$ \mathbf{q} -grid. (b) $\text{P}\bar{1}$ with $2 \times 2 \times 2$ \mathbf{k} -grid and $1 \times 1 \times 1$ \mathbf{q} -grid. (c) $\text{I}\bar{4}2\text{m}$ with $3 \times 3 \times 3$ \mathbf{k} -grid $2 \times 2 \times 2$ \mathbf{q} -grid. (d) $\text{Cmc}2_1$ with $3 \times 3 \times 3$ \mathbf{k} -grid and $2 \times 2 \times 2$ \mathbf{q} -grid.

We also present their X-ray diffraction in Fig. S8 of the SI which show large differences that can easily be resolved experimentally. We also present their phonon dispersion and phonon DOS in Fig. 2. Remarkably, the two perovskites structures, Figs. 2(a) and (b), show a continuous spectra with phonon frequencies below 150 cm^{-1} while the two non-perovskite structures show multiple localized and high-energy vibrational modes up to 180 cm^{-1} , see Figs. 2(c) and (d). In particular, both show the same iodine localized vibrational peak at 120 cm^{-1} which is characteristic of these structures.

These differences can be explained by studying their crystal structure, shown in Fig. 3. The two structures shown in Figs. 3(c) and (d) cannot be classified as double perovskites as both cation sites (K and In in this case) are not in an octahedral coordination environments as the cubic phase of Cs_2KInI_6 . Indeed, the In cation is in a tetrahedral environment, while the geometry of the K cation is not well-defined; it is coordinated with six I atoms in $\text{I}\bar{4}2\text{m}$ and seven I atoms in $\text{Cmc}2_1$. For the $\text{P}3̄$

structure, our CHEMENV analysis gives 100% octahedral similarity with a slightly distorted octahedron for the K cations. Finally, in the $\text{P}\bar{1}$ structure, the K cations do not exhibit an octahedral environment. However, CHEMENV reports a combination of different coordinations for each K site, see Fig. S9 of the SI. From this analysis, the $\text{P}3̄$ (147) phase is classified as a double perovskite while the case of the $\text{P}\bar{1}$ structure is more complex since the In cations are octahedrally coordinated while the K cations are not. Since the $\text{P}3̄$ structure is classified as a double perovskite, we compare it with the cubic phase. In the latter, the In and K octahedra share corners in all three directions, forming a three-dimensional alternating network, see Fig. 3(a). In the trigonal phase, they share faces instead of corners, see Fig. 3(b), producing one-dimensional strips in which the In and K octahedra alternate. This change from a three-dimensional corner-sharing network to one-dimensional face-sharing strips reflects a significant reduction in structural connectivity.

We now turn to the analysis of the impact of structural

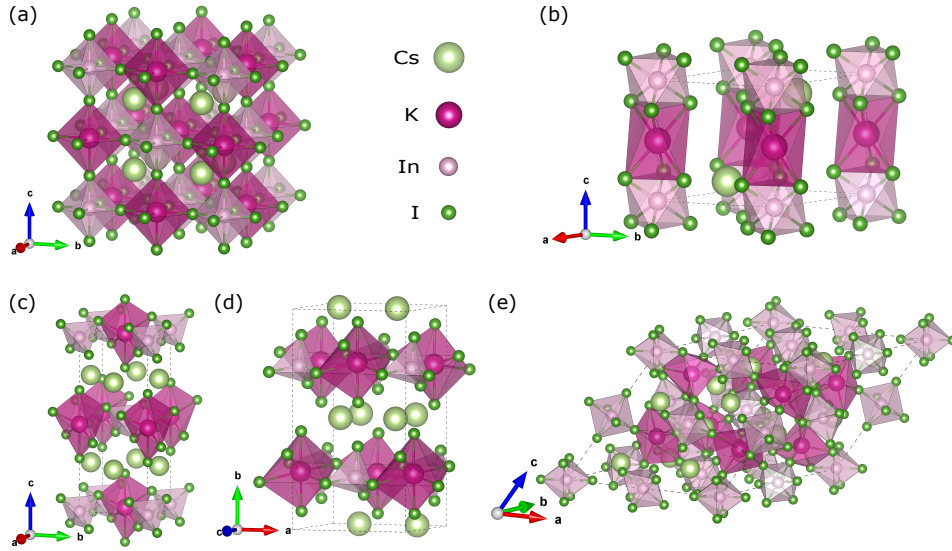


FIG. 3. Crystal structures of (a) $Fm\bar{3}m$, (b) $P\bar{3}$, (c) $I\bar{4}2m$, (d) $Cmc2_1$ and (e) $P\bar{1}$, displaying the coordination environments of In and K cations and the way they are connected.

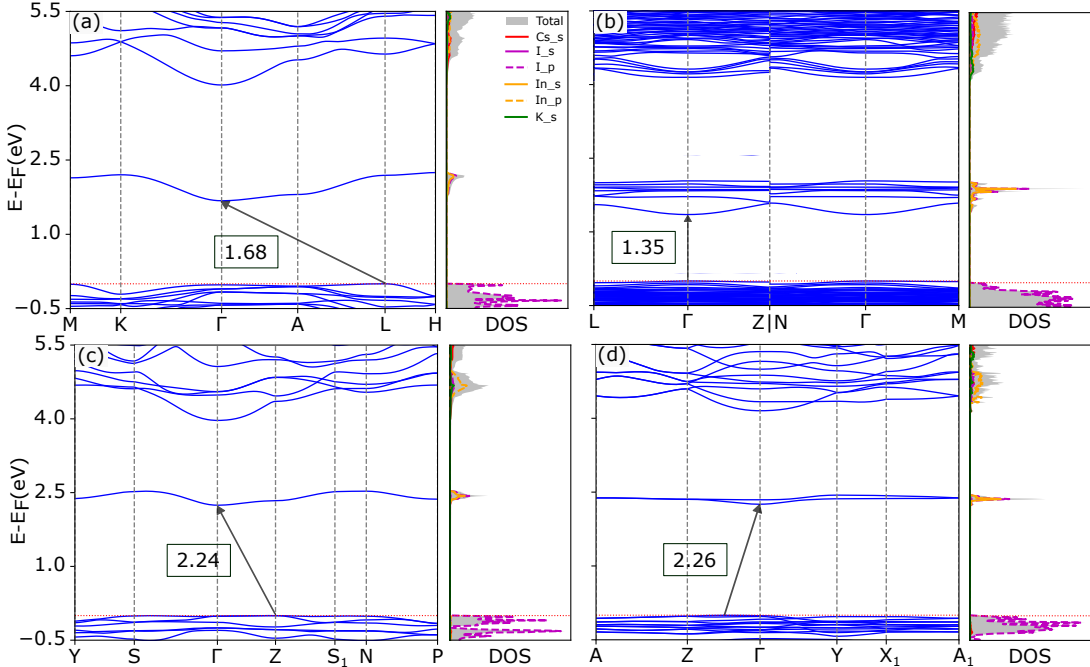


FIG. 4. Electronic structure of dynamically stable phases of Cs_2KInI_6 : (a) $P\bar{3}$, (b) $P\bar{1}$, (c) $I\bar{4}2m$, and (d) $Cmc2_1$. The energies are expressed with respect to the Fermi level (E_F), located at the valence band maximum.

differences on electronic properties. Figure 4 presents the electronic structure of the four investigated phases of Cs_2KInI_6 while that of the cubic phase is presented in Fig. S10 of the SI. That reference phase shows a direct band gap of 1.24 eV at the Γ point. The valence band at the high symmetry point M is only 13 meV lower than the valence band maximum (VBM) at Γ . In the four considered cases, the band gap increases as a result of structural distortions, most notably changes in the In and K coordination environments and the connectivity

of their octahedra. These distortions also change the band gap from direct in the cubic phase to indirect in all other phases, except for $P\bar{1}$. The double perovskite structure, $P\bar{3}$ has an indirect band gap of 1.68 eV, see Fig. 4(a). However, the valence band at the Γ point is approximately 20 meV lower than the VBM. This gap is only slightly larger than that of the cubic phase. The structure $P\bar{1}$ in which only the In cations form octahedrons has a direct band gap of 1.35 eV, see Fig. 4(b), which is close to that of the cubic phase and could be

TABLE II. Effective masses of electron and hole for the dynamically stable phases of Cs_2KInI_6 along with the high symmetry cubic phase. The valence band maximum (VBM) and the conduction band minimum (CBM) are also reported. For the $\text{Cmc}2_1$ structure, the VBM does not lie at a high-symmetry point and is indicated with a star (*).

Space group		VBM	CBM	Direction	m_e^*	m_h^*
Fm $\bar{3}$ m	225	Γ	Γ	$\Gamma - L$	0.345	2.068
P $\bar{3}$	147	L	Γ	$\Gamma - K$	0.345	2.690
				$\Gamma - A$	1.458	—
				$\Gamma - K$	0.546	—
				$L - A$	—	4.478
P $\bar{1}$	2	Γ	Γ	$L - H$	—	0.552
				$\Gamma - Z$	0.523	2.706
				$\Gamma - L$	0.577	1.651
I $\bar{4}2m$	121	Z	Γ	$\Gamma - Z$	1.476	—
				$\Gamma - S$	0.635	—
				$Z - \Gamma$	—	16.636
				$Z - S_1$	—	4.645
Cmc 2_1	36	*	Γ	$\Gamma - Y$	0.772	—
				$\Gamma - Z$	1.167	—
				$* - \Gamma$	—	5.519
				$* - Z$	—	5.344

promising for solar cell applications. The valence band at the M point is 12 meV lower than the VBM at Γ . The I $\bar{4}2m$ and Cmc 2_1 structures that are not classified as double perovskites have significantly larger band gaps than the cubic phase: 2.24 eV and 2.26 eV, respectively. Both are indirect band gaps, with the valence band at the Γ point lying only slightly below the VBM about 11 meV for I $\bar{4}2m$ and 0.5 meV for Cmc 2_1 . Overall, structural distortions increase the band gap and flatten the conduction and valence bands, thereby increasing the effective electron and hole masses, as reported in Table II.

We investigate the structural stability and electronic properties of lead-free halide double perovskite Cs_2KInI_6 using first-principles calculations and the machine-learned interatomic potential MACE. Phonon calculations reveal that the high-symmetry cubic phase is dynamically unstable. To find lower-energy stable configurations, we applied a genetic algorithm along unstable phonon eigenmodes, yielding 42 stable candidates according to finite-displacement phonon calculations with MACE. Selected structures were further validated by DFPT to address possible MLIP inaccuracies. We focus

on four stable phases: P $\bar{3}$, I $\bar{4}2m$, Cmc 2_1 , and P $\bar{1}$, classified by the coordination of In and K cations and their octahedral connectivity. The most stable phases, I $\bar{4}2m$ and Cmc 2_1 , are not double perovskites, as In is tetrahedrally coordinated and the K environment is ambiguous. P $\bar{3}$ is a double perovskite, whereas P $\bar{1}$ is less clearly so: In is octahedrally coordinated but K is not. Electronic-structure calculations show that distortions increase the band gap relative to the cubic phase and usually change it from direct to indirect. The cubic phase has a direct band gap of 1.24 eV, near the optimal photovoltaic value. The double-perovskite P $\bar{3}$ phase has an indirect band gap of 1.68 eV, with the valence band at Γ only slightly below the VBM. The P $\bar{1}$ phase is the most promising for photovoltaics, retaining a direct band gap of 1.35 eV. Overall, Cs_2KInI_6 exhibits multiple dynamically stable phases, from double to non-double perovskites, with varying octahedral connectivity in the double-perovskite structures. These transformations significantly modify the electronic properties, clarifying structure–property relationships in halide double perovskites and demonstrating the effectiveness of combining machine-learned interatomic potentials with genetic algorithms to discover novel stable phases in complex materials.

ACKNOWLEDGMENTS

G.-M.R. is Research Director of the Fonds de la Recherche Scientifique - FNRS. S. P. is a Research Associate of the Fonds de la Recherche Scientifique - FNRS. This work was supported by the Fonds de la Recherche Scientifique - FNRS under Grants number T.0183.23 (PDR) and T.W011.23 (PDR-WEAVE). This publication was supported by the Walloon Region in the strategic axe FRFS-WEL-T. V. T. acknowledges support from the FRS-FNRS through a FRIA Grant. Computational resources have been provided by the Consortium des Équipements de Calcul Intensif (CÉCI), funded by the Fonds de la Recherche Scientifique de Belgique (F.R.S.-FNRS) under Grant No. 2.5020.11 and by the Walloon Region. The present research benefited from computational resources made available on the Tier-1 supercomputer of the Fédération Wallonie-Bruxelles, infrastructure funded by the Walloon Region under grant agreement n°1117545.

[1] M. H. Miah, M. U. Khandaker, M. B. Rahman, M. Nur-E-Alam, and M. A. Islam, Band gap tuning of perovskite solar cells for enhancing the efficiency and stability: issues and prospects, *RSC Advances* **14**, 15876–15906 (2024).

[2] S. De Wolf, J. Holovsky, S.-J. Moon, P. Löper, B. Niesen, M. Ledinsky, F.-J. Haug, J.-H. Yum, and C. Ballif, Organometallic halide perovskites: Sharp optical absorp-

tion edge and its relation to photovoltaic performance, *The Journal of Physical Chemistry Letters* **5**, 1035–1039 (2014).

[3] A. Chilvery, S. Das, P. Guggilla, C. Brantley, and A. Sunda-Meya, A perspective on the recent progress in solution-processed methods for highly efficient perovskite solar cells, *Science and Technology of Advanced Materials* **17**, 650–658 (2016).

[4] National Renewable Energy Laboratory, Best research-cell efficiency chart, <https://www.nrel.gov/pv/cell-efficiency> (2025), accessed: 2025-06-16.

[5] Y. Zhao and K. Zhu, Organic-inorganic hybrid lead halide perovskites for optoelectronic and electronic applications, *Chemical Society Reviews* **45**, 655–689 (2016).

[6] S. Poncé, M. Schlipf, and F. Giustino, Origin of low carrier mobilities in halide perovskites, *ACS Energy Letters* **4**, 456–463 (2019).

[7] C. Q. Xia, J. Peng, S. Poncé, J. B. Patel, A. D. Wright, T. W. Crothers, M. Uller Rothmann, J. Borchert, R. L. Milot, H. Kraus, Q. Lin, F. Giustino, L. M. Herz, and M. B. Johnston, Limits to electrical mobility in lead-halide perovskite semiconductors, *The Journal of Physical Chemistry Letters* **12**, 3607–3617 (2021).

[8] G. E. Eperon, G. M. Paternò, R. J. Sutton, A. Zampetti, A. A. Haghaghirad, F. Cacialli, and H. J. Snaith, Inorganic caesium lead iodide perovskite solar cells, *Journal of Materials Chemistry A* **3**, 19688–19695 (2015).

[9] M. Lyu, J. Yun, P. Chen, M. Hao, and L. Wang, Addressing toxicity of lead: Progress and applications of low-toxic metal halide perovskites and their derivatives, *Advanced Energy Materials* **7**, 1602512 (2017).

[10] Y.-H. Kye, C.-J. Yu, U.-G. Jong, Y. Chen, and A. Walsh, Critical role of water in defect aggregation and chemical degradation of perovskite solar cells, *The Journal of Physical Chemistry Letters* **9**, 2196–2201 (2018).

[11] U.-G. Jong, C.-J. Yu, G.-C. Ri, A. P. McMahon, N. Harrison, P. R. F. Barnes, and A. Walsh, Influence of water intercalation and hydration on chemical decomposition and ion transport in methylammonium lead halide perovskites, *Journal of Materials Chemistry A* **6**, 1067–1074 (2018).

[12] A. H. Slavney, T. Hu, A. M. Lindenberg, and H. I. Karunadasa, A bismuth-halide double perovskite with long carrier recombination lifetime for photovoltaic applications, *Journal of the American Chemical Society* **138**, 2138–2141 (2016).

[13] G. Volonakis, M. R. Filip, A. A. Haghaghirad, N. Sakai, B. Wenger, H. J. Snaith, and F. Giustino, Lead-free halide double perovskites via heterovalent substitution of noble metals, *The Journal of Physical Chemistry Letters* **7**, 1254–1259 (2016).

[14] C. N. Savory, A. Walsh, and D. O. Scanlon, Can pb-free halide double perovskites support high-efficiency solar cells?, *ACS Energy Letters* **1**, 949–955 (2016).

[15] T. Li, S. Luo, X. Wang, and L. Zhang, Alternative lone-pair ns^2 -cation-based semiconductors beyond lead halide perovskites for optoelectronic applications, *Advanced Materials* **33**, 2008574 (2021).

[16] E. T. McClure, M. R. Ball, W. Windl, and P. M. Woodward, Cs_2AgBiX_6 ($X = Br, Cl$): New visible light absorbing, lead-free halide perovskite semiconductors, *Chemistry of Materials* **28**, 1348–1354 (2016).

[17] Y. Cai, W. Xie, Y. T. Teng, P. C. Harikesh, B. Ghosh, P. Huck, K. A. Persson, N. Mathews, S. G. Mhaisalkar, M. Sherburne, and M. Asta, High-throughput computational study of halide double perovskite inorganic compounds, *Chemistry of Materials* **31**, 5392–5401 (2019).

[18] A. Jain, S. P. Ong, G. Hautier, W. Chen, W. D. Richards, S. Dacek, S. Cholia, D. Gunter, D. Skinner, G. Ceder, and K. A. Persson, Commentary: The materials project: A materials genome approach to accelerating materials innovation, *APL Materials* **1**, 1–11 (2013).

[19] F. Qi, X. Lv, J. Song, X. Fu, L. Meng, and C.-Z. Lu, Optoelectronic performance of perovskite Cs_2KMI_6 ($M = Ga, In$) based on high-throughput screening and first-principles calculations, *Physical Chemistry Chemical Physics* **25**, 11484–11492 (2023).

[20] R. L. Z. Hoye, J. Hidalgo, R. A. Jagt, J. Correa-Baena, T. Fix, and J. L. MacManus-Driscoll, The role of dimensionality on the optoelectronic properties of oxide and halide perovskites, and their halide derivatives, *Advanced Energy Materials* **12**, 2100499 (2021).

[21] P. Hohenberg and W. Kohn, Inhomogeneous electron gas, *Physical Review* **136**, B864–B871 (1964).

[22] W. Kohn and L. J. Sham, Self-consistent equations including exchange and correlation effects, *Physical Review* **140**, A1133–A1138 (1965).

[23] P. Giannozzi, O. Andreussi, T. Brumme, O. Bunau, M. Buongiorno Nardelli, M. Calandra, R. Car, C. Cavazzoni, D. Ceresoli, M. Cococcioni, N. Colonna, I. Carnimeo, A. Dal Corso, S. de Gironcoli, P. Delugas, R. A. DiStasio, A. Ferretti, A. Floris, G. Fratesi, G. Fugallo, R. Gebauer, U. Gerstmann, F. Giustino, T. Gorni, J. Jia, M. Kawamura, H.-Y. Ko, A. Kokalj, E. Küçükbenli, M. Lazzari, M. Marsili, N. Marzari, F. Mauri, N. L. Nguyen, H.-V. Nguyen, A. Otero-de-la Roza, L. Paulatto, S. Poncé, D. Rocca, R. Sabatini, B. Santra, M. Schlipf, A. P. Seitsonen, A. Smogunov, I. Timrov, T. Thonhauser, P. Umari, N. Vast, X. Wu, and S. Baroni, Advanced capabilities for materials modelling with quantum espresso, *Journal of Physics: Condensed Matter* **29**, 465901 (2017).

[24] J. P. Perdew, K. Burke, and M. Ernzerhof, Generalized gradient approximation made simple, *Physical Review Letters* **77**, 3865–3868 (1996).

[25] M. van Setten, M. Giantomassi, E. Bousquet, M. Verstraete, D. Hamann, X. Gonze, and G.-M. Rignanese, The pseudodojo: Training and grading a 85 element optimized norm-conserving pseudopotential table, *Computer Physics Communications* **226**, 39–54 (2018).

[26] H. J. Monkhorst and J. D. Pack, Special points for brillouin-zone integrations, *Physical Review B* **13**, 5188–5192 (1976).

[27] X. Gonze and C. Lee, Dynamical matrices, born effective charges, dielectric permittivity tensors, and interatomic force constants from density-functional perturbation theory, *Phys. Rev. B* **55**, 10355 (1997).

[28] S. Baroni, S. de Gironcoli, A. Dal Corso, and P. Giannozzi, Phonons and related crystal properties from density-functional perturbation theory, *Reviews of Modern Physics* **73**, 515–562 (2001).

[29] M. Bercx, S. Poncé, Y. Zhang, G. Trezza, A. G. Ghezeljehmeidan, L. Bastonero, J. Qiao, F. O. von Rohr, G. Pizzi, E. Chiavazzo, and N. Marzari, Charting the landscape of bardeen-cooper-schrieffer superconductors in experimentally known compounds, *PRX Energy* **4**, 033012 (2025).

[30] I. Batatia, D. P. Kovács, G. N. C. Simm, C. Ortner, and G. Csányi, *Mace: Higher order equivariant message passing neural networks for fast and accurate force fields* (2022).

[31] I. Batatia, S. Batzner, D. P. Kovács, A. Musaelian, G. N. C. Simm, R. Drautz, C. Ortner, B. Kozinsky, and G. Csányi, The design space of e(3)-equivariant atom-centred interatomic potentials, *Nature Machine Intelligence* **7**, 56–67 (2025).

[32] D. Waroquiers, J. George, M. Horton, S. Schenk, K. A.

Persson, G.-M. Rignanese, X. Gonze, and G. Hautier, Chemenv: a fast and robust coordination environment identification tool, *Acta Crystallographica Section B Structural Science, Crystal Engineering and Materials* **76**, 683–695 (2020).

[33] U.-G. Jong, C.-J. Yu, Y.-H. Kye, S.-H. Choe, J.-S. Kim, and Y.-G. Choe, Anharmonic phonons and phase transitions in the vacancy-ordered double perovskite Cs_2SnI_6 from first-principles predictions, *Physical Review B* **99**, 184105 (2019).

[34] J. Yin, O. Hellman, and S. Poncé, Impact of anharmonicity on the carrier mobility of the pb-free CsSnBr_3 perovskite, *Phys. Rev. B* **112**, L140303 (2025).

[35] R. A. Gouvêa and G.-M. Rignanese, *VIBROML* (2026), GitHub repository.

SI: From Symmetry to Stability: Structural and Electronic Transformation in Cs_2KInI_6

Mohammad Bakhsh¹, Victor Trinquet¹, Rogério Almeida Gouvêa¹, Gian-Marco Rignanese^{1,2}, and Samuel Poncé^{1,2}

¹ *UCLouvain, Institute of Condensed Matter and Nanosciences (IMCN),*

Chemin des Étoiles 8, B-1348 Louvain-la-Neuve, Belgium and

² *WEL Research Institute, avenue Pasteur 6, 1300 Wavre, Belgium.*

Table S1. Polymorphs of Cs_2KInI_6 which are stable according to MACE, with relative total energy (ΔE in meV/atom), band gap (E_g in eV), and stability predicted with DFPT.

id	Space group	N_{at}	ΔE	E_g	Stability with DFPT
00	$\text{Fm}\bar{3}\text{m}$	225	10	0.0	1.24
01	$\text{P}2$	3	10	-9.1	1.76
02	$\text{P}\bar{1}$	2	10	-22.1	1.95
03	$\text{P}\bar{3}1\text{m}$	162	10	-22.1	1.95
04	$\text{C}2/\text{m}$	12	10	-24.8	1.60
05	$\text{P}\bar{3}$	147	10	-30.8	1.66
06	$\text{C}2$	5	10	-34.2	2.24
07	$\text{I}\bar{4}2\text{m}$	121	10	-34.2	2.24
08	$\text{P}\bar{1}$	2	20	-6.8	1.26
09	$\text{P}2_1/\text{c}$	14	20	-13.7	1.58
10	$\text{P}\bar{1}$	2	20	-14.4	1.19
11	$\text{P}\bar{1}$	2	20	-16.8	1.78
12	$\text{P}\bar{1}$	2	20	-17.2	2.00
13	$\text{P}\bar{1}$	2	20	-17.8	1.82
14	$\text{P}\bar{1}$	2	20	-18.0	1.93
15	$\text{P}\bar{1}$	2	20	-18.1	1.78
16	$\text{P}\bar{1}$	2	20	-19.1	1.98
17	$\text{P}\bar{1}$	2	20	-20.4	1.85
18	$\text{P}\bar{1}$	2	20	-20.4	1.83
19	$\text{P}\bar{1}$	2	20	-22.3	1.83
20	$\text{P}\bar{1}$	2	20	-23.8	2.16
21	$\text{P}\bar{1}$	2	20	-24.2	2.00
22	$\text{P}\bar{1}$	2	20	-24.7	2.08
23	$\text{P}\bar{1}$	2	20	-25.0	1.94
24	$\text{P}\bar{1}$	2	20	-27.9	2.08
25	$\text{P}\bar{1}$	2	20	-28.1	1.87
26	$\text{P}\bar{1}$	2	20	-29.1	1.97
27	$\text{P}\bar{1}$	2	20	-30.2	2.37
28	$\text{P}\bar{1}$	2	20	-30.8	2.08
29	$\text{P}\bar{1}$	2	20	-30.9	1.67
30	$\text{P}\bar{1}$	2	20	-31.3	2.20
31	$\text{P}\bar{1}$	2	20	-31.7	1.68
32	Cmcm	63	20	-34.3	2.15
33	$\text{P}\bar{1}$	2	20	-34.5	1.89
34	$\text{C}2/\text{m}$	12	20	-36.1	2.31
35	$\text{P}\bar{1}$	2	20	-36.1	2.31
36	$\text{Ama}2$	40	20	-39.7	2.28
37	$\text{Cmc}2_1$	36	20	-41.9	2.26
38	$\text{P}\bar{1}$	2	40	-24.4	1.93
39	$\text{P}\bar{1}$	2	40	-26.3	2.25
40	$\text{P}\bar{1}$	2	40	-28.0	1.36
41	Pc	7	40	-39.7	2.28
42	$\text{P}\bar{1}$	2	80	-30.4	1.35

Table S2. Polymorphs of Cs_2KInI_6 unstable according to MACE and DFPT, with relative total energy (ΔE in meV/atom), and band gap (E_g in eV).

id	Space group	N_{at}	ΔE	E_g
00	$\text{Fm}\bar{3}\text{m}$	225	10	0.0
43	$\text{R}\bar{3}$	148	10	-17.1
44	$\text{C}2/\text{m}$	12	10	-22.0
45	$\text{C}2/\text{m}$	12	10	-29.5
46	$\text{Fmm}2$	42	10	-34.4
47	Cm	8	10	-34.4

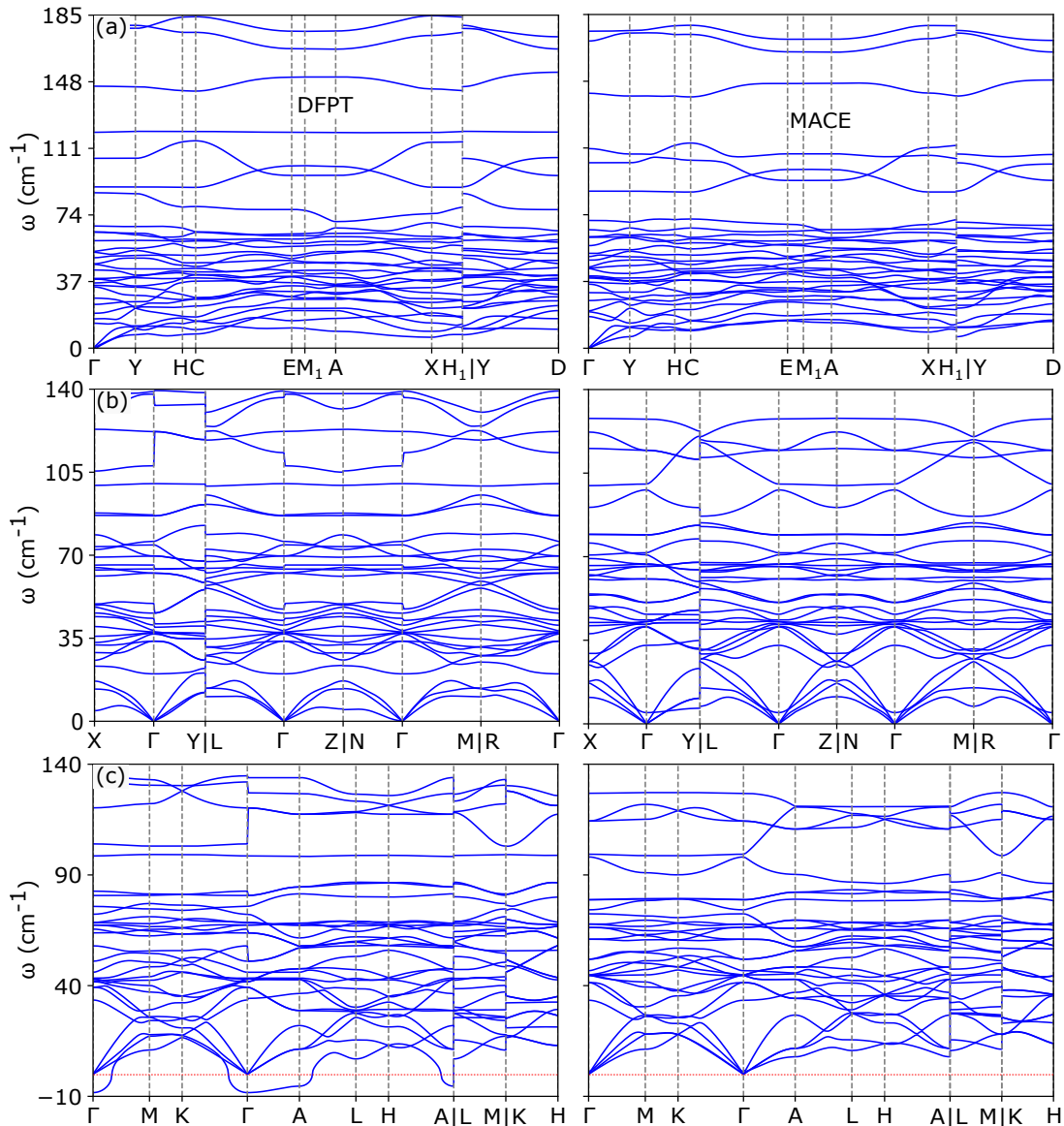


Figure S1. Phonon dispersions from DFPT (left) and finite displacement with MACE (right) for Cs_2KInI_6 phases with id numbers from Table S1. All MACE calculations use a displacement of 0.01 \AA . (a) id=01 with $4 \times 8 \times 4$ \mathbf{k} -grid and $2 \times 4 \times 2$ \mathbf{q} -grid (DFPT), and a $4 \times 7 \times 3$ supercell (MACE). (b) id=02 with $8 \times 6 \times 8$ \mathbf{k} -grid and $4 \times 3 \times 4$ \mathbf{q} -grid (DFPT), and $5 \times 4 \times 5$ supercell (MACE). (c) id=03 with $4 \times 4 \times 4$ \mathbf{k} -grid and $2 \times 2 \times 2$ \mathbf{q} -grid (DFPT), and a $4 \times 4 \times 4$ supercell (MACE).

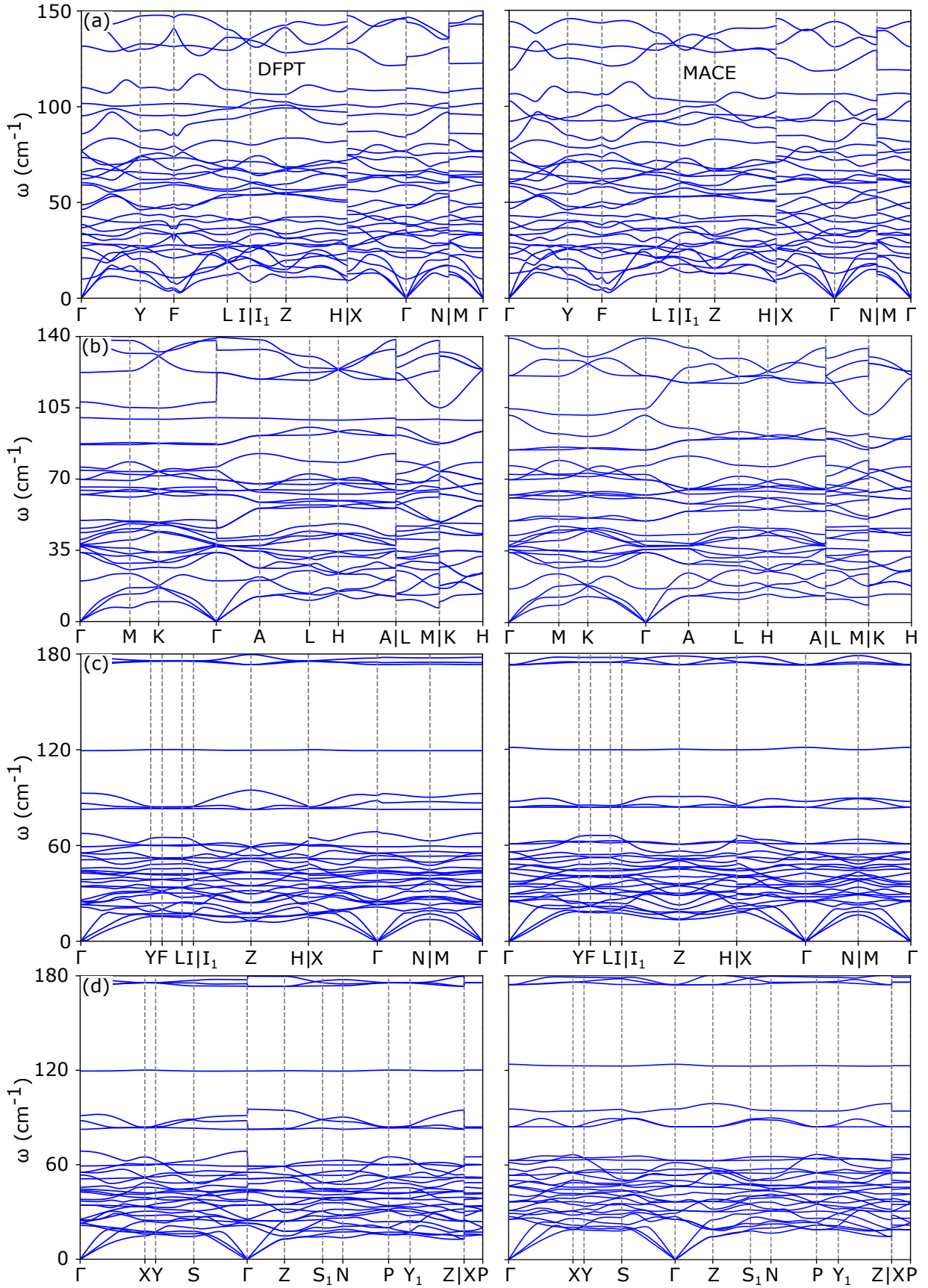


Figure S2. Phonon dispersions from DFPT (left) and finite displacement with MACE (right) for Cs_2KInI_6 phases with id numbers from Table S1. All MACE calculations use a displacement of 0.01 \AA . (a) id=04 with $4 \times 4 \times 4$ \mathbf{k} -grid and $2 \times 2 \times 2$ \mathbf{q} -grid (DFPT), and a $5 \times 5 \times 5$ supercell (MACE). (b) id=05 with $4 \times 4 \times 4$ \mathbf{k} -grid and $2 \times 2 \times 2$ \mathbf{q} -grid, and a $5 \times 5 \times 5$ supercell (MACE). (c) id=06 with $4 \times 4 \times 6$ \mathbf{k} -grid and $2 \times 2 \times 3$ \mathbf{q} -grid (DFPT), and a $3 \times 3 \times 5$ supercell (MACE). (d) id=07 with $3 \times 3 \times 3$ \mathbf{k} -grid and $2 \times 2 \times 2$ \mathbf{q} -grid (DFPT), and a $5 \times 5 \times 5$ supercell (MACE).

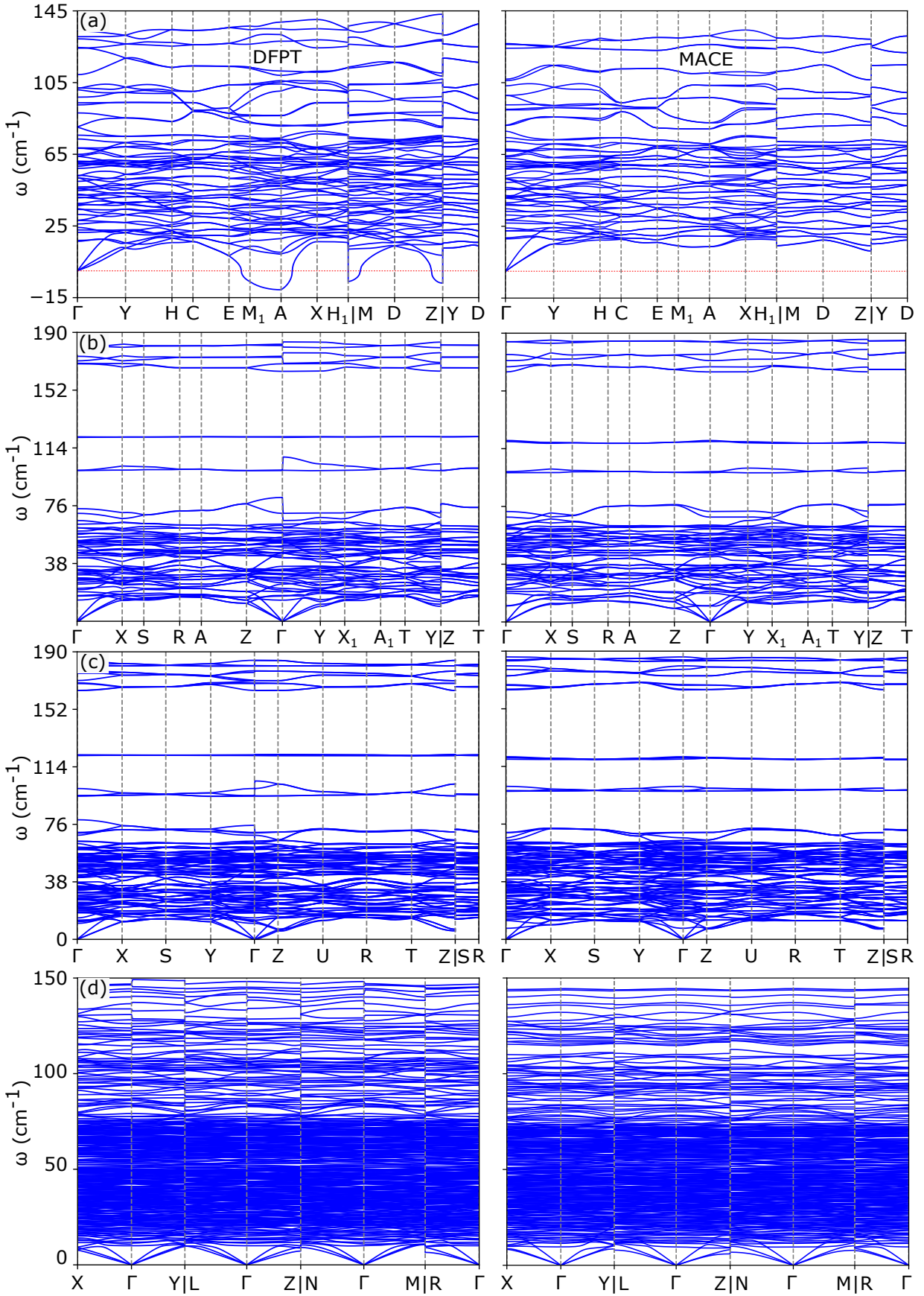


Figure S3. Phonon dispersions from DFPT (left) and finite displacement with MACE (right) for Cs_2KInI_6 phases with id numbers from Table S1. All MACE calculations use a displacement of 0.01 \AA . (a) id=09 with $4 \times 2 \times 4$ \mathbf{k} -grid and $2 \times 1 \times 2$ \mathbf{q} -grid (DFPT), and a $4 \times 3 \times 4$ supercell (MACE). (b) id=37 with $3 \times 3 \times 3$ \mathbf{k} -grid and $2 \times 2 \times 2$ \mathbf{q} -grid (DFPT), and a $3 \times 3 \times 3$ supercell (MACE). (c) id=41 with $4 \times 4 \times 2$ \mathbf{k} -grid and $2 \times 2 \times 2$ \mathbf{q} -grid (DFPT), and a $4 \times 4 \times 3$ supercell (MACE). (d) id=42 with $2 \times 2 \times 2$ \mathbf{k} -grid and $1 \times 1 \times 1$ \mathbf{q} -grid (DFPT), and a $3 \times 3 \times 3$ supercell (MACE).

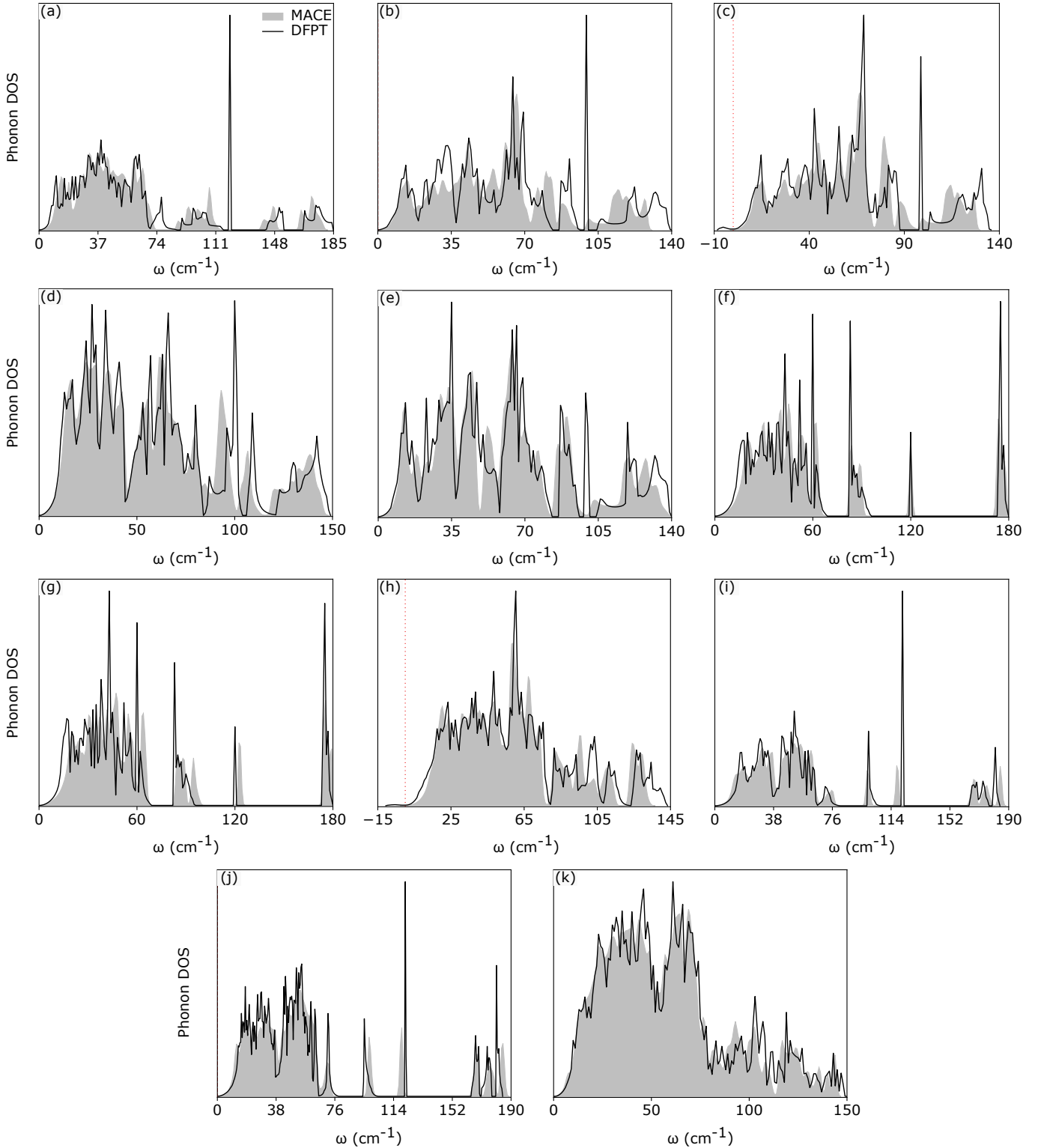


Figure S4. Phonon density of states (PDOS) obtained from DFPT and the finite-displacement method using MACE for Cs_2KInI_6 phases with id numbers listed in Table S1. The corresponding phonon band dispersions are shown in Figures S1, S2, and S3. A $40 \times 40 \times 40$ q-point grid was used to compute the PDOS, except for the structures with 40 (id=41) and 80 (id=42) atoms, for which $30 \times 30 \times 30$ and $15 \times 15 \times 15$ grids were used, respectively. The PDOS were normalized by the area under the curve within a common frequency range shared by the DFPT and MACE results. (a) id=01, (b) id=02, (c) id=03, (d) id=04, (e) id=05, (f) id=06, (g) id=07, (h) id=09, (i) id=37, (j) id=41, (k) id=42.

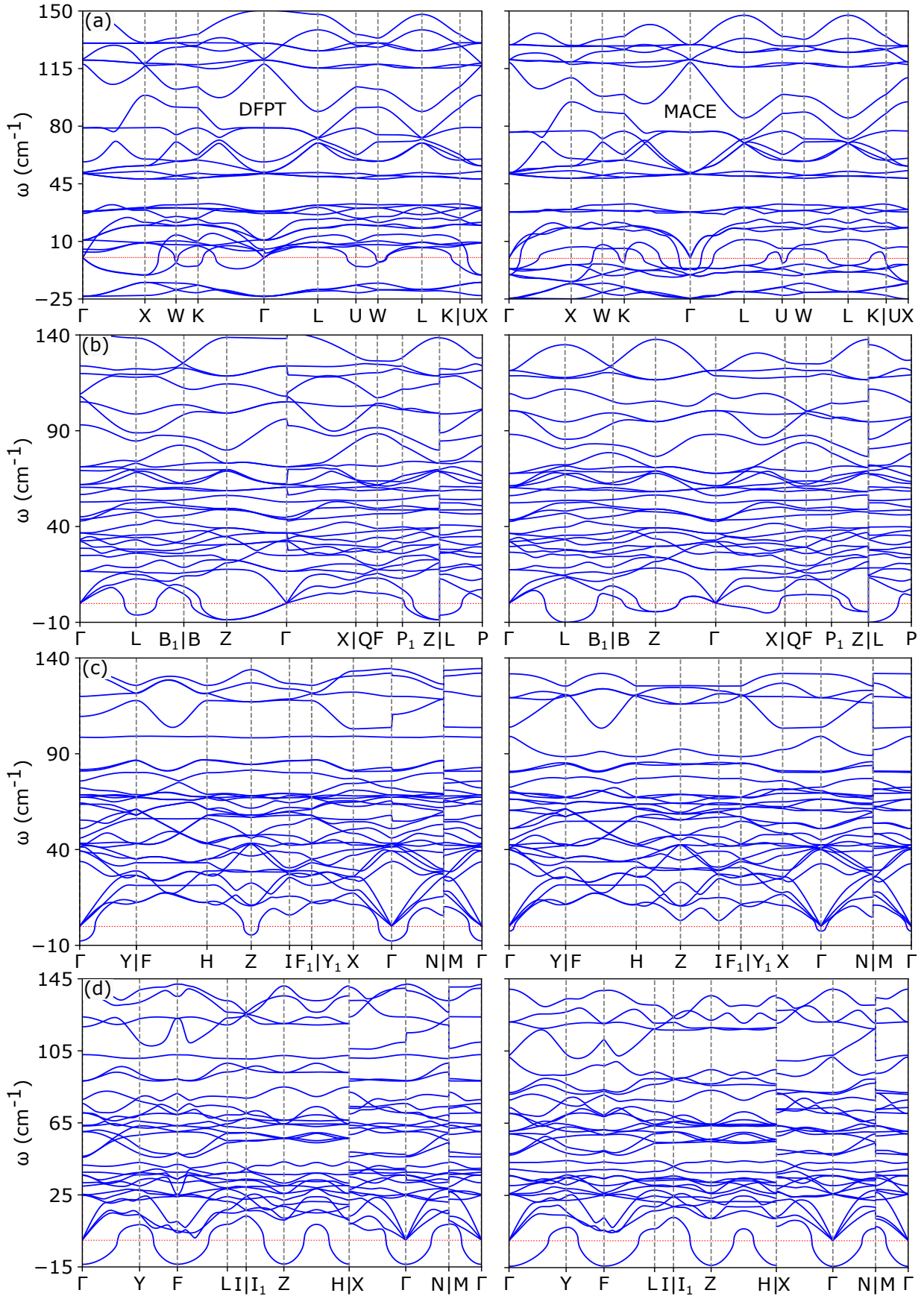


Figure S5. Phonon dispersions from DFPT (left) and finite displacement with MACE (right) for Cs_2KInI_6 phases with id numbers from Table S2. All MACE calculations use a displacement of 0.01 \AA . (a) id=00 with $3 \times 3 \times 3$ \mathbf{k} -grid and $2 \times 2 \times 2$ \mathbf{q} -grid (DFPT), and a $3 \times 3 \times 3$ supercell (MACE). (b) id=43 with $3 \times 3 \times 3$ \mathbf{k} -grid and $2 \times 2 \times 2$ \mathbf{q} -grid (DFPT), and a $5 \times 5 \times 5$ supercell (MACE). (c) id=44 with $6 \times 6 \times 4$ \mathbf{k} -grid and $3 \times 3 \times 2$ \mathbf{q} -grid (DFPT), and $6 \times 6 \times 4$ supercell (MACE). (d) id=45 with $4 \times 4 \times 4$ \mathbf{k} -grid and $2 \times 2 \times 2$ \mathbf{q} -grid (DFPT), and a $5 \times 5 \times 5$ supercell (MACE).

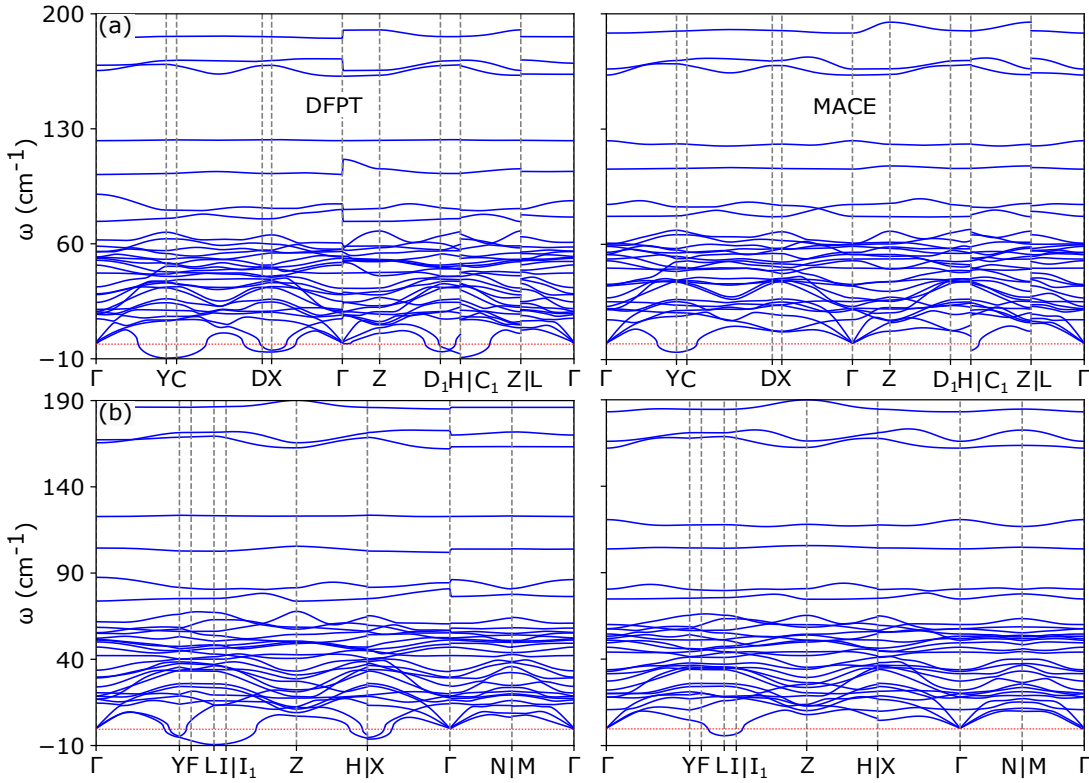


Figure S6. Phonon dispersions from DFPT (left) and finite displacement with MACE (right) for Cs_2KInI_6 phases with id numbers from Table S2. All MACE calculations use a displacement of 0.01 \AA . (a) id=46 with $4 \times 4 \times 6$ \mathbf{k} -grid and $2 \times 2 \times 3$ \mathbf{q} -grid (DFPT), and a $5 \times 5 \times 7$ supercell (MACE). (b) id=47 with $6 \times 6 \times 4$ \mathbf{k} -grid and $3 \times 3 \times 2$ \mathbf{q} -grid (DFPT), and a $5 \times 5 \times 3$ supercell (MACE).

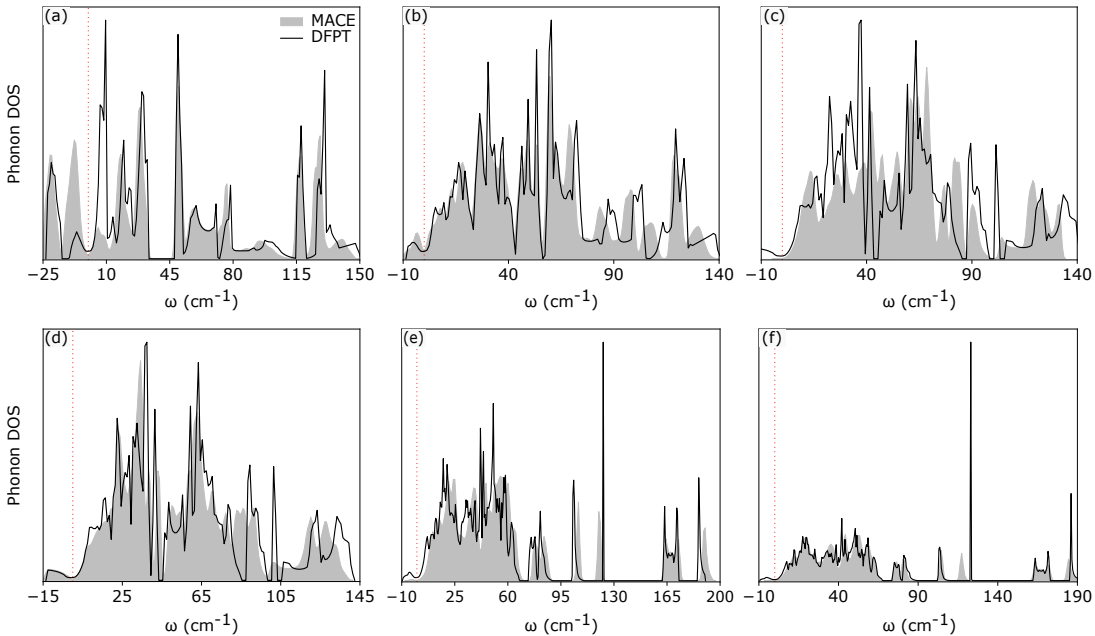


Figure S7. Phonon density of states (PDOS) obtained from DFPT and the finite-displacement method using MACE for Cs_2KInI_6 phases with id numbers listed in Table S2. The corresponding phonon band dispersions are shown in Figures S5 and S6. A $40 \times 40 \times 40$ q-point grid was used to compute the PDOS. The PDOS were normalized by the area under the curve within a common frequency range shared by the DFPT and MACE results. (a) id=00, (b) id=43, (c) id=44, (d) id=45, (e) id=46, (f) id=47.

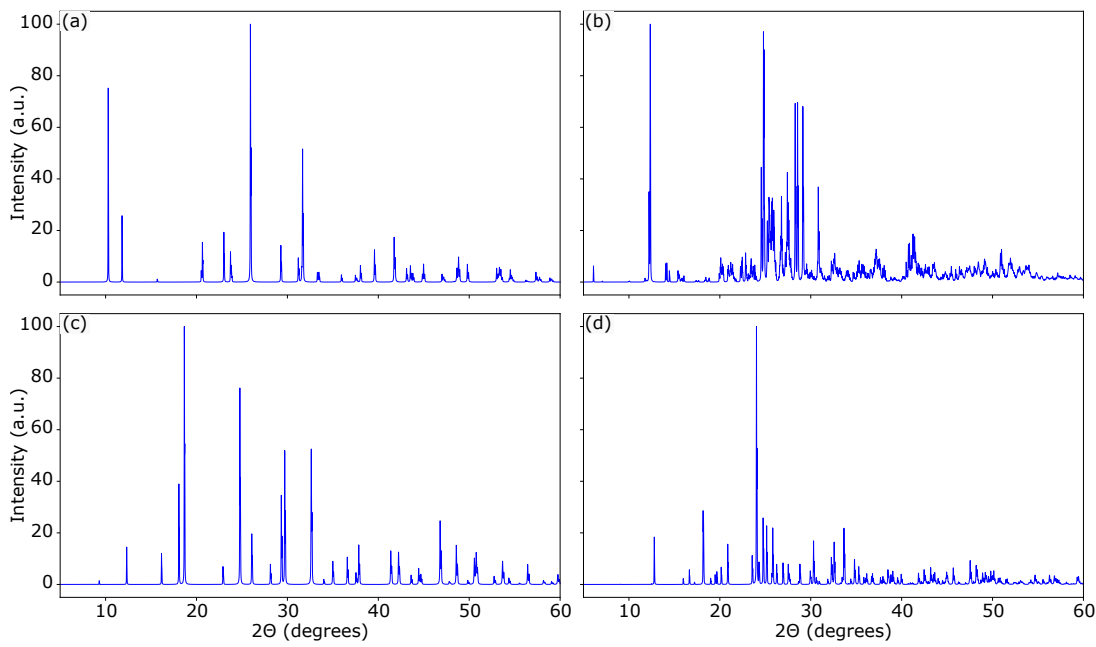


Figure S8. X-ray powder diffractogram of four dynamically stable Cs_2KInI_6 phases, obtained from VESTA with X-rays of wave length 1.54 \AA . (a) $\text{P}3$ (147), (b) $\text{P}1$ (2), (c) $\text{I}42\text{m}$ (121), (d) $\text{Cmc}2_1$ (36).

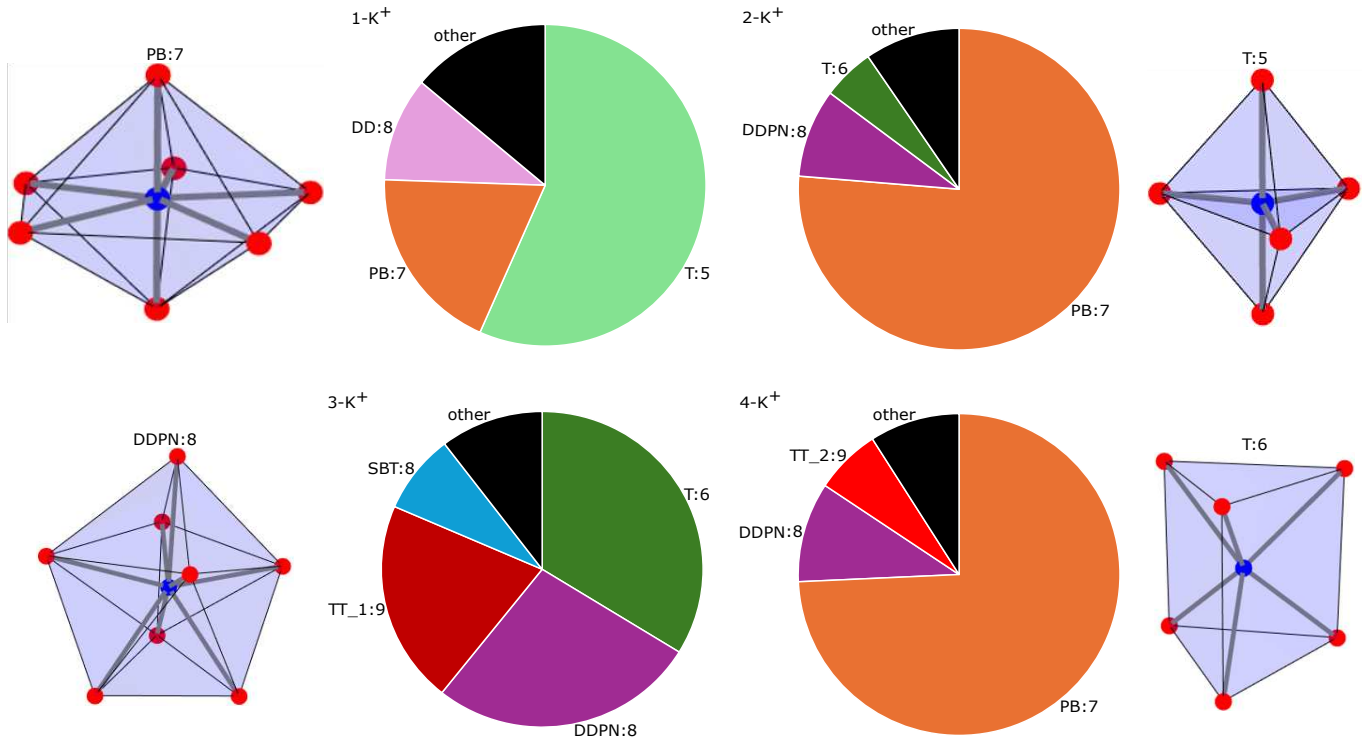


Figure S9. Analysis of the coordination environments of K cations for $\text{P}1$ (2): T:5 = Trigonal bipyramidal, PB:7 = Pentagonal bipyramidal, T:6 = Trigonal prism, DD:8 = Dodecahedron with triangular faces, DDPN:8 = Dodecahedron with triangular faces – p2345 plane normalized, TT_1:9 = Tricapped triangular prism (three square-face caps), TT_2:9 = Tricapped triangular prism (two square-face caps and one triangular-face cap), SBT:8 = Square-face bicapped trigonal prism.

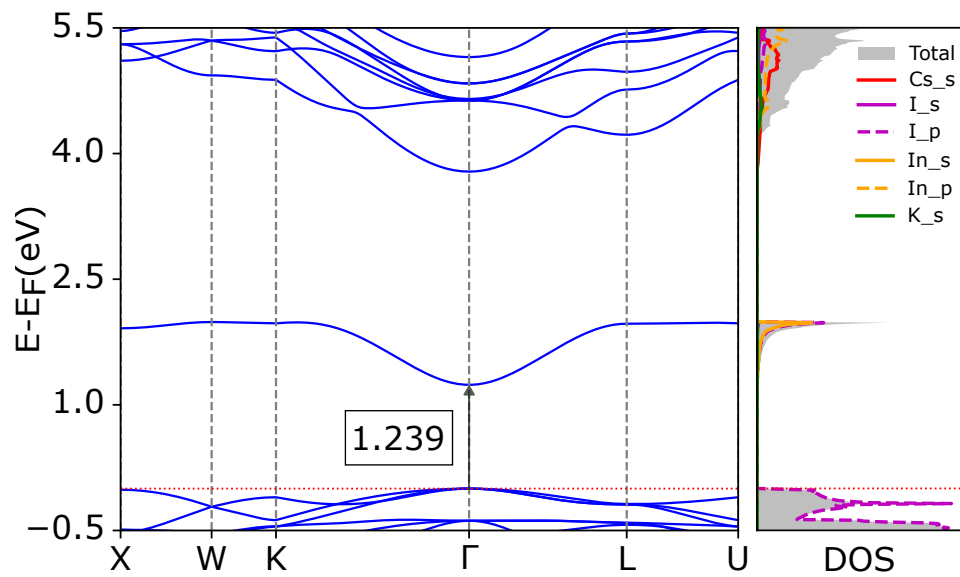


Figure S10. Electronic structure and density of states of Cs_2KInI_6 for the high-symmetry unstable phase $\text{Fm}\bar{3}\text{m}$ (225)